Progress In Electromagnetics Research B, Vol. 25, 131–154, 2010

THE LEVEL SET SHAPE RECONSTRUCTION ALGORITHM APPLIED TO 2D PEC TARGETS HIDDEN BEHIND A WALL

M. R. Hajihashemi and M. El-Shenawee

University of Arkansas
Fayetteville, USA

Abstract—The level set algorithm is extended to handle the reconstruction of the shape and location of objects hidden behind a dielectric wall. The Green's function of stratified media is used to modify the method of moments and the surface integral equation forward solver. Due to the oscillatory nature of the Sommerfeld integrals, the stationary phase approximation is implemented here to achieve fast and accurate reconstruction results, especially when the targets are located adequately far from the wall. Transverse Magnetic (TM) plane waves are employed for excitation with limited view for transmitting and receiving the waves in the far field at one side of the wall. The results show the capability of the level set method for retrieving the shape and location of multiple 2D PEC objects of arbitrary shapes even when there are located at a small distance from the wall. To reduce the computational expenses of the algorithm in the case of multiple hidden objects, the MPI parallelization technique is implemented leading to a reduction in the CPU time from hours on a single processor to few minutes using 128 processors on the NCSA Supercomputer Center.

1. INTRODUCTION

The electromagnetic waves have the ability to penetrate through nonmetallic walls made of wood, glass, brick, and/or concrete blocks. The reflected waves could be analyzed to reconstruct the profile and the location of hidden objects behind these walls. The through-wall imaging is challenging because of the complex multiple scattering mechanisms that occur between the objects and the dielectric wall.

Received 26 July 2010, Accepted 23 August 2010, Scheduled 25 August 2010
Corresponding author: M. R. Hajihashemi (mhajihas@uark.edu).

Examples of applications include earthquake and fire rescue operations, police search operations, homeland security, and military applications as reported in several work in the literature [1–19]. The reported results in [1–17] were based on permittivity reconstruction of hidden objects behind a wall, while works in [18–20] were focused on the shape reconstruction of hidden objects.

In [1], a subspace-based optimization method was applied for through-wall imaging. The target objects of different profiles were well reconstructed even in the presence of high level of noise in the data. In [2], a through-the-wall imaging technique based on time reversal method was introduced for the detection of moving targets in a cluttered environment. In [3], a simple procedure to detect changes in a through-the-wall imaging scenario was reported validated against synthetic and experimental data. In [4], a microwave imaging technique that combined the FDTD method and the Polak-Ribière algorithm for reconstructing underground multiple scatterers was presented. In [5], the characterization of inclusions in concrete structures using the matched-filter-based reverse-time (MFBRT) migration algorithm and the particle swarm optimization (PSO) was investigated.

Most of the accomplished works in this field were based on synthetic aperture radar (SAR) and ultra-wideband (UWB) radar techniques [8, 9]. In [10], a 2-D contrast source inverse scattering method was applied in a multilayered medium and a high-quality image reconstruction was achieved using multi-frequency data with a limited array view.

The Born approximation was employed for qualitative reconstruction of hidden 2-D objects behind the wall [7, 17]. The algorithm was tested using synthetic and experimental data; however, the method was restricted to canonical scatterers. A synthetic aperture array technique was presented for imaging the targets behind the wall using ultra wideband antennas and wide range of incidence angles [8]. A 3-D ultra wideband SAR technique for surface reconstructing of hidden objects using real data was implemented achieving a reduction in the calculation time [9].

Another 3-D through-the-wall beam former based on applying a transformation to bring the target and the transmitter/receiver to the same height was designed [11]. A two-step imaging procedure by means of a linear inverse scattering technique was presented for imaging the objects behind a wall whose parameters were not completely known [12]. A wideband beam forming-based technique was proposed to perform imaging with wall parameter ambiguities and different standoff distances [13, 14]. The signature of a metallic target behind a thick brick wall was obtained using low frequencies and a monostatic

approach [15]. The application of spatial filters to suppress, or drastically mitigate the wall reflections, was proposed in [16]. Some work suggested estimating the wall parameters based on the model of a dielectric slab and the early arrival time [12].

In [18], the Kirchhoff approximation was employed for shape reconstruction of perfectly conducting objects when the scattering data were collected in a finite region around the targets. The linear sampling method was employed for the inverse problem of non-accessible targets concealed into a wall or under a floor [19].

Most of the above works provided only the contrast of the hidden object with respect to the background medium but did not provide the shape of these targets. Although the current work assumes *a priori* knowledge of the dielectric wall's constitutive parameters and thickness, which could be a realistic assumption in several applications, the proposed level set algorithm provides the exact shape of the hidden targets and also their locations. The level set inversion method has shown a potential in shape reconstruction as reported in the literature [20–24]. In a relevant work by Ramananjaona et al., the level set technique was used for reconstructing the shape of 2-D obstacles buried in a half-space of low dielectric material using both transverse magnetic (TM) and transverse electric (TE) polarizations [20]. Most of the reported results were restricted to monochromatic data and rectangular shaped objects.

The level set is an implicit mathematical framework for the shape reconstruction problems in electromagnetics, more in depth details given in [20–29]. The numerical results demonstrate the capability of the method for handling the topological changes (i.e., breaking and merging of the region). A simple initial guess can evolve to several objects during the reconstruction scheme.

The level set technique is implemented in this work to reconstruct the location and the shape of multiple PEC objects of arbitrary shapes hidden behind a known dielectric wall. The challenge in the current work is the implementation of the Green's function in stratified media in the level set algorithm [26, 27]. An approximation of the Green's function using the stationary phase method is implemented to reduce the CPU time without much sacrificing of the accuracy.

The stationary phase method (saddle point method) is found to be an effective approach for the fast calculation of the Sommerfeld integrals in stratified media. The calculation time for the MoM impedance matrix in stratified media is almost in the same order of that in free space. The accuracy of the method is validated using different examples shown in Section 2.4. The obtained reconstruction results demonstrate the efficiency of the algorithm especially when the

target objects are not placed too close to the wall.

Plane wave illumination of the wall with TM polarization indicates that the electric field is parallel to the cylinders' axes. Several multiple scattering mechanisms contribute to the received waves such as the scattering from the objects, the scattering from the dielectric wall, and the multiple scattering between the objects and the wall as discussed in Section 2. The constitutive parameters and the thickness of the wall are assumed to be *a priori* known which allows the offline calculation of their effect on the scattered waves. However, the multiple scattering between the unknown objects and the wall cannot *a priori* be predicted. In the case of inhomogeneous wall, closed-form expressions to take into account the wall effect are not generally available. In this case, numerical techniques such as finite difference methods could be applicable. As reported in [12], there are some statistical methods to deal with the through-the-wall imaging under ambiguous wall parameters.

2. METHODOLOGY

2.1. Level Set Representation

We assume that the moving contour $\Gamma(t)$ is represented implicitly as the zero level of a two-dimensional function $\Phi(\cdot)$, as shown in the two dimensional configuration (2-D) in Fig. 1. At each time t, the interface is represented as [28]:

$$\Gamma(t) = \{(x, y) \,|\Phi(x, y, t) = 0\} \tag{1}$$

Upon obtaining the derivative of (1) with respect to the evolving time t, we have the following expression for tracking the motion of the interface known as the Hamilton-Jacobi equation [28, 29]:

$$\frac{\partial}{\partial t}\Phi(x, y, t) + F(\bar{r}) \, \|\nabla\Phi(x, y, t)\| = 0 \tag{2a}$$

$$\Phi_0 = \Phi(x, y, t = 0) \tag{2b}$$

where $F(\cdot)$ is the normal component of the deformation velocity on the contour (see Fig. 1). The objective here is to minimize the cost function which is the mismatch error between the simulated scattered far-field of the evolving objects during the inversion process and the scattered far-field of the true object (data) [21]. The appropriate form of the deformation velocity, making a decreasing cost function, was given in [22]. It was based on the forward and adjoint currents induced on the surface of the evolving objects [30].

The PDE in (2) is solved numerically using the higher order finite difference schemes elaborated in [28]. If the value of the level set

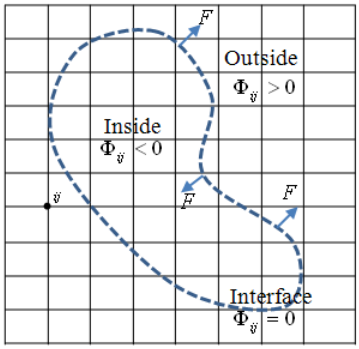

Figure 1. Implicit representation of the evolving contour using level set.

function Φ at any grid point (x_i, y_j), at any time $n\Delta t$, is denoted by the symbol $\Phi_{ij}^n = \Phi(x_i, y_j, n\Delta t)$, the updated value of the level set function at time $(n+1)\Delta t$ is calculated as follows [28]:

$$\Phi_{ij}^{n+1} = \Phi_{ij}^n - \Delta t \left[\max(F_{ij}, 0)\nabla^+ + \min(F_{ij}, 0)\nabla^-\right] \tag{3a}$$

where $F_{ij} = F(x_i, y_j)$ represents the velocity function at (x_i, y_j). The symbols ∇^+ and ∇^- are given as follows [28]:

$$\nabla^+ = \left(\max(D_{ij}^{x-}, 0) + \min(D_{ij}^{x+}, 0) + \max(D_{ij}^{y-}, 0) + \min(D_{ij}^{y+}, 0)\right)^{1/2} \tag{3b}$$

$$\nabla^- = \left(\min(D_{ij}^{x-}, 0) + \max(D_{ij}^{x+}, 0) + \min(D_{ij}^{y-}, 0) + \max(D_{ij}^{y+}, 0)\right)^{1/2} \tag{3c}$$

The directional derivatives of the level set functions in (3) are calculated, for example, as follows:

$$D_{ij}^{y+} = \frac{\Phi(x_i, y_j + \Delta y) - \Phi(x_i, y_j)}{\Delta y} \tag{3d}$$

$$D_{ij}^{x-} = \frac{\Phi(x_i, y_j) - \Phi(x_i - \Delta x, y_j)}{\Delta x} \tag{3e}$$

The function $\Phi_0(\cdot)$ is the signed distance function, shortest distance between a grid point and the contour, corresponding to the initial guess. The choice of the signed distance function avoids steep gradients and rapidly changing features during the inversion algorithm [29]. The time step required for solving the PDE given in (1) is chosen according to the Courant-Friedrichs-Lewy (CFL) stability condition which asserts that the numerical wave should propagate at least as fast as the physical waves [28, 29]. The level set shape

reconstruction algorithm in the stratified media is similar to that of the free space reported in [21] except that the forward scattering problem is more computationally demanding in the stratified media due to the need to numerically evaluate the Sommerfeld integration. The modified forward scattering problem and the choice of the deformation velocity are discussed as follows.

2.2. Forward Scattering Problem in a Stratified Media

This work is based on the configuration of Fig. 2 where a known homogenous dielectric wall with the relative permittivity ε_r and conductivity σ is located at $-h < x < 0$ in the x-y plane.

A time-varying line source carrying a current $I = 1$ A with angular frequency $\omega = 2\pi f$ is located at (x', y') in the half space $x > 0$ parallel to the z-axis. The electric field, which is the Green's function of the stratified media, at any point (x, y) in $x > 0$ region is produced as follows, assuming time convention of $e^{j\omega t}$ [26, 27]:

$$\begin{aligned} G(x,y;x',y') &= \frac{\omega\mu_0}{4\pi j}\int_{-\infty}^{+\infty}\frac{e^{-j\xi(y-y')}}{u(\xi)}\left(e^{-u(\xi)|x-x'|}+R^-(k_0,\xi)e^{-u(\xi)(x+x')}\right)d\xi \\ &= -\frac{\omega\mu_0}{4}H_0^{(2)}\left(k_0\sqrt{(x-x')^2+(y-y')^2}\right) \\ &\quad +\frac{\omega\mu_0}{4\pi j}\int_{-\infty}^{+\infty}\frac{e^{-j\xi(y-y')}}{u(\xi)}R^-(k_0,\xi)e^{-u(\xi)(x+x')}d\xi \end{aligned} \tag{4a}$$

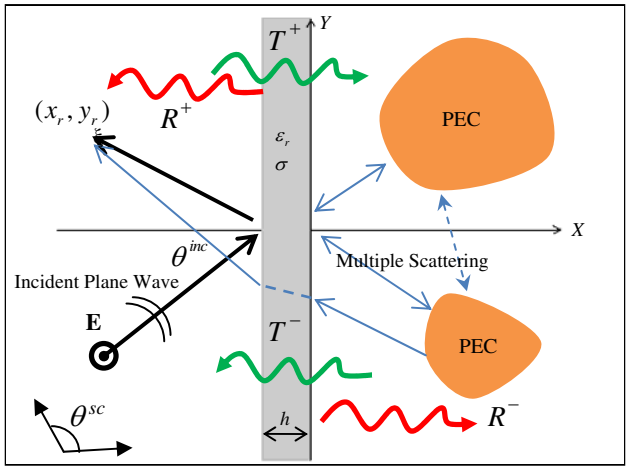

Figure 2. Configuration of hidden objects behind a dielectric wall.

where $u(\xi) = \sqrt{\xi^2 - k_0^2}$ is the phase factor and $H_0^{(2)}(\cdot)$ is the zero order Hankel's function of the second kind. The symbol k_0 represents the free space wave number. The symbol of ε_0 represents the permittivity of the free space and the symbol of μ_0 represents the permeability of the free space. The term $R^-(k_0, \xi)$, the wall reflection coefficient at $x > 0$, is given by [26]:

$$R^-(k_0, \xi) = \frac{\left(u_1 u_3 - u_2^2\right) \sinh(u_2 h)}{u_2(u_1 + u_3)\cosh(u_2 h) + \left(u_1 u_3 + u_2^2\right)\sinh(u_2 h)} \tag{4b}$$

with $u_1 = u_3 = \sqrt{\xi^2 - k_0^2}$ and $u_2 = \sqrt{\xi^2 - k_0^2 \tilde{\varepsilon}_r}$. The symbol $\tilde{\varepsilon}_r$ is the effective dielectric permittivity of the dielectric wall with thickness h given by [26]

$$\tilde{\varepsilon}_r = \varepsilon_r + \frac{\sigma}{j\omega\varepsilon_0} \tag{5}$$

In this work, we assume that multiple perfectly electric conducting (PEC) infinite cylinders with arbitrary cross-sections and total contour C (that represents the contours of all objects) are located in the half space $x > 0$. The induced current on the surface of the conducting cylinders has only the z-component $J_z^{ind}(x', y')$. Upon enforcing the boundary condition for the total electric field to vanish on the surface of the PEC objects, the following integral equation is obtained to be solved for the induced current using the Method of Moments (MoM) [27].

$$\int_C J_z^{ind}\left(x', y'\right) G\left(x, y; x', y'\right) dl' = -E_z^t(x, y) \tag{6}$$

where $G(x, y; x', y')$ is the Green's function in the stratified media given by (4a) and $E_z^t(x, y)$ is the transmitted incident electric field at any point $(x, y) \in C$ given by [27]:

$$E_z^t(x, y) = T^+(k_0, k_0 \sin\theta_i) e^{-jk_0(x\cos\theta_i + y\sin\theta_i)} \tag{7}$$

where $T^+(k_0, k_0 \sin\theta_i)$ is the transmission coefficient through the dielectric wall given by [26]:

$$T^+(k_0, \xi) = \frac{2u_1 u_2 e^{u_1 h}}{u_2(u_1 + u_3)\cosh(u_2 h) + \left(u_1 u_3 + u_2^2\right)\sinh(u_2 h)} \tag{8}$$

Upon calculating the induced current on the surface of conducting cylinders, the scattered electric field due to the PEC objects, $E_{z,O}^{scat}(x_r, y_r)$, at any receiver point (x_r, y_r) at $x < -h$ region is given

by [27]:

$$E^{sc}_{z,O}(x_r, y_r) = \frac{\omega\mu_0}{4\pi j} \int_C J^{ind}_z\left(x', y'\right) \int_{-\infty}^{+\infty} \frac{T^-(k_0, \xi) e^{-j\xi(y_r - y')}}{u(\xi)} e^{u(\xi)(h + x_r - x')} d\xi dl' \quad (9)$$

where $T^-(k_0, \xi)$ is the transmission coefficient through the dielectric wall given by [26]:

$$T^-(k_0, \xi) = \frac{2u_1 u_2}{u_2(u_1 + u_3)\cosh(u_2 h) + \left(u_1 u_3 + u_2^2\right)\sinh(u_2 h)} \quad (10)$$

The total scattered field, which is due to the wall and the objects, in (x_r, y_r) is given by [27]:

$$E^{sc}_{z,total}(x_r, y_r) = E^{sc}_{z,wall}(x_r, y_r) + E^{sc}_{z,O}(x_r, y_r) \quad (11)$$

where $E^{sc}_{wall}(x_r, y_r)$ is the scattered field from the dielectric wall in the absence of the PEC objects and it is given by [26]

$$E^{sc}_{wall}(x_r, y_r) = R^+(k_0, k_0 \sin\theta_i) e^{jk_0(x_r \cos\theta_i - y_r \sin\theta_i)} \quad (12)$$

where $R^+(k_0, k_0 \sin\theta_i)$ is the reflection coefficient from the dielectric wall given by [26]:

$$R^+(k_0, \xi) = R^-(k_0, \xi) e^{2u_1 h} \quad (13)$$

The far field pattern of the scattered field from the objects represented by $E^{scat}_O(\cdot)$ will be used in the level set algorithm. Since the constitutive parameters of the dielectric wall and its thickness are *a priori* known, the contribution of the wall to the total scattered field is $E^{scat}_{wall}(x_r, y_r)$ for certain incident direction θ^{inc} can be calculated offline using (12). If the point receiver (x_r, y_r) is adequately far from the dielectric wall (300λ is assumed in this work), the far-field pattern from objects, $P^{sc}_{z,O}(\theta^{inc}, \theta^{sc})$ in the direction of θ^{sc} is calculated as follows [21]:

$$P^{sc}_{z,O}(\theta^{inc}, \theta^{sc}) = \sqrt{\rho}\, e^{jk_0\rho} E^{sc}_{z,O}(x_r, y_r) \quad (14)$$

where $\rho = \sqrt{x_r^2 + y_r^2}$ and $\theta^{sc} = \tan^{-1}(\frac{y_r}{x_r})$ (see Fig. 2). The deformation velocity $F(\cdot)$ in (2) is the same as in [22] where the conducting cylinders were immersed in free space with no walls. In general, the formulation of the deformation velocity was obtained upon minimizing the mismatch between the scattered far fields of the

evolving objects and the true targets (defined as the cost function). The expression of the deformation velocity F is given in [22]:

$$F(\bar{r}) = -\alpha \,\mathrm{Re}\Bigg[e^{-i\frac{\pi}{4}} \sum_{i=1}^{N_I} \sum_{j=1}^{N_M(i)} \left(E^{sc}_{z,sim}(\theta_i^{inc}, \theta_{ij}^{meas}) - E^{sc}_{z,meas}(\theta_i^{inc}, \theta_{ij}^{meas})\right)^* J_z(\bar{r}).J'_z(\bar{r})\Bigg] \tag{15}$$

where N_I is the number of incident waves, $N_M(i)$ is the number of measurements under the ith incidence, θ_i^{inc} is the ith incident angle, θ_{ij}^{meas} is the mth measurement angle for θ_i^{inc}, $J_z(\bar{r})$ is the induced current solution of the forward problem and $J'_z(\bar{r})$ is the induced current solution of the adjoint problem [30]. The symbols $E^{sc}_{z,sim}$ and $E^{sc}_{z,meas}$ represent the calculated and the measured scattered fields, respectively, and α is a positive normalization coefficient.

The main constraint for the shape reconstruction of the objects behind the wall is that the incident and scattered waves are limited to certain views as shown in Fig. 2, unlike the free space configuration. These constraints are given by:

$$-\frac{\pi}{2} < \theta^{inc} < \frac{\pi}{2}, \quad \text{and} \quad \frac{\pi}{2} < \theta^{sc} < \frac{3\pi}{2} \tag{16}$$

The angles are measured with respect to the positive x-direction as shown in Fig. 2. Therefore, it is challenging to retrieve the details in parts of the targets where the illumination is not available similar to the concept of shadowing.

2.3. Stationary Phase method

The calculation of the Sommerfeld integral in stratified media is computationally challenging, but the stationary phase method is employed to approximate the integration in (4a) [31]. The integrand in (4a) has a rapidly oscillating behavior due to the exponential term $e^{-j\xi(y-y')-u(\xi)(x+x')}$ while the reflection coefficient $R^-(k_0, \xi)$ has a slowly varying behavior compared to the exponential part. Therefore, the latter can be replaced by its value at the stationary point $\xi = \xi_1$ where,

$$\frac{\partial}{\partial \xi}\left[-j\xi\left(y-y'\right) - \sqrt{\xi^2 - k_0^2}\left(x+x'\right)\right]_{\xi=\xi_1} = 0 \Rightarrow \tag{17a}$$

$$\xi_1 = \frac{k_0(y-y')}{\sqrt{(x+x')^2 + (y-y')^2}} \tag{17b}$$

The second term in (4a) can be approximated as follows:

$$\begin{aligned}
&\frac{\omega\mu_0}{4\pi j}\int_{-\infty}^{+\infty}\frac{e^{-j\xi(y-y')}}{u(\xi)}R^-(k_0,\xi)e^{-u(\xi)(x+x')}d\xi \\
\approx\ & R^-(k_0,\xi_1)\frac{\omega\mu_0}{4\pi j}\int_{-\infty}^{+\infty}\frac{e^{-j\xi(y-y')}}{\sqrt{\xi^2-k_0^2}}e^{-\sqrt{\xi^2-k_0^2}(x+x')}d\xi \\
=\ & R^-(k_0,\xi_1)\frac{\omega\mu_0}{4\pi j}\int_{-\infty}^{+\infty}\frac{e^{-j\xi(y-y')}}{\sqrt{\xi^2-k_0^2}}e^{-\sqrt{\xi^2-k_0^2}(x+x')}d\xi \\
=\ & \frac{-\omega\mu_0}{4}R^-(k_0,\xi_1)H_0^{(2)}\left(k_0\sqrt{(x+x')^2+(y-y')^2}\right) \qquad (18)
\end{aligned}$$

A Similar approach is employed to approximate the integral of (9). The first step is to find the stationary point of the rapidly varying exponential part as:

$$\frac{\partial}{\partial\xi}\left[-j\xi\left(y_r-y'\right)-\sqrt{\xi^2-k_0^2}\left(h+x_r-x'\right)\right]_{\xi=\xi_2}=0\Rightarrow \qquad (19a)$$

$$\xi_2=\frac{k_0(y_r-y')}{\sqrt{(h+x_r-x')^2+(y_r-y')^2}} \qquad (19b)$$

The slowly varying part in (9) can be replaced by its value at the stationary point as follows:

$$E^{sc}_{z,O}(x_r,y_r)\approx\frac{\omega\mu_0}{4\pi j}\int_C J_z^{ind}(x',y')T^-(k_0,\xi_2)\int_{-\infty}^{+\infty}\frac{e^{-j\xi(y_r-y')}}{u(\xi)}e^{u(\xi)(h+x_r-x')}d\xi dl'$$

$$=-\frac{\omega\mu_0}{4}\int_C J_z^{ind}(x',y')T^-(k_0,\xi_2)H_0^{(2)}\left(k_0\sqrt{(h+x_r-x')^2+(y_r-y')^2}\right)dl' \qquad (20)$$

The scattered field is calculated in the far field zone which justifies the approximation in (19). Compared with other numerical methods, the level-set algorithm based on the MoM provides more efficient reconstruction results, since calculating the scattered fields and the deformation velocity requires the calculation of the induced currents only on the contour of the evolving objects. Furthermore the deformation velocity is directly calculated on the moving contours and then extended to the whole computational domain [21–25].

In most of the inverse scattering techniques, the scattered field in a single frequency does not provide enough information for retrieving the details of the target objects. In this work after a pre-assigned number of iterations (e.g., 1000 iterations), the working frequency hops to a higher one to retrieve finer details of the unknown objects [21].

2.4. Validation of the Forward Solver

The accuracy of the forward solver in the stratified medium is investigated using (i) the full Green's function in (4a), (ii) the same expression but with ignoring the second term in (4a), and (iii) using the stationary phase method (19), (20). The validation is conducted at different frequencies and different distances of the object from the wall. The numerical results are compared with the commercial EM-simulator FEKO [32].

In the first example, the scattered electric field due to a circular PEC cylinder with a radius of $r_c = 20\,\text{cm}$ centered at $(x_c, y_c) = (50\,\text{cm}, 0)$ is shown in Fig. 3. Normal incidence is considered $\theta^{inc} = 0$ at frequency of $f = 1\,\text{GHz}$. The thickness of the wall is assumed 20 cm made of a material with $\varepsilon_r = 2.2$ and loss tangent $\tan\delta = 0.001$. The point receivers are placed at $x_r = -2m$ and $1\,\text{m} < y_r < 1\,\text{m}$. Fig. 4 shows the magnitude of the scattered electric fields due to the objects $E^{sc}_{z,O}(x_r, y_r)$ (9) using the full Green's function (4a), the Green's function upon ignoring the second term in (4a), the stationary phase method (20), and FEKO. The results show that the stationary phase method demonstrates very good agreement with using both FEKO and the full Green's function (4a). However, ignoring the interaction between the dielectric wall and the object (i.e., ignoring the second term in (4a)) causes an error of 3% compared to the full Green's function in this case.

As expected, the multiple scattering between the objects and the wall, which is represented by the second term in (4a), increases as the distance between the wall and the objects decreases. The phase results show similar validation but are not presented here. Another validation was conducted using the same circular PEC cylinder but when located closer to the wall at $(x_c, y_c) = (25\,\text{cm}, 0)$ with the permittivity of the wall $\varepsilon_r = 4.5$. In this case and compared with the results of Fig. 4, the

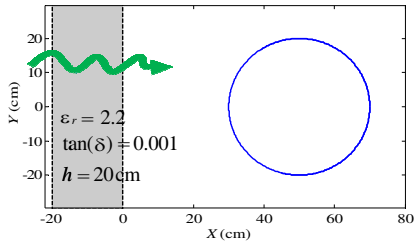

Figure 3. Circular cylinder with the radius of 20 cm.

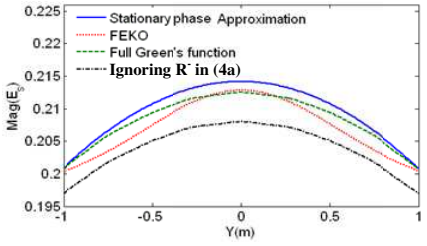

Figure 4. Scattered electric field from the circular cylinder.

error between using the full Green's function and the stationary phase method has increased to 4%; the error between using the full Green's function and FEKO has increased to 11%; and the error between using the full Green's function and the same expression but with ignoring the R^- term in (4a) has increased to 25% (plots are not shown).

As observed in Fig. 10(d), if the target is placed close to the wall, the reconstruction results are not very accurate; this is a common problem in see through wall imaging. In this case, the assumption that the source (wall) and the observation point (target) to be adequately far from each other does not hold. Alternatively, other more time consuming techniques, such as complex image method, could be used [34].

The CPU time required when using the full Green's function is ~ 38 min total, ~ 16 min when ignoring the second term in (4a), while it is only 2 sec when using the stationary phase method. For FEKO, the simulation of the structure of Fig. 3 required several hours since it was modeled as a 3-D electromagnetic scattering problem. Based on the above, the stationary phase method will be used in all results of Section 4 for generating the synthetic data and for calculating the scattered fields of the evolving objects during the inversion process.

3. NUMERICAL RESULTS

3.1. Reconstruction of Two Elliptical Cylinders

In the first case, the reconstruction of two elliptical PEC cylinders located behind a lossless dielectric wall is examined. The thickness of the wall is assumed $h = 50\,\text{cm}$ with the permittivity of $\varepsilon_r = 2.2$. The semi-major and semi-minor axes lengths of the ellipises are $a = 6\,\text{cm}$ and $b = 2\,\text{cm}$, respectively. The separation distance between the two ellipses is 40 cm measured between their centers. The two ellipses are located at (40 cm, 20 cm) and (40 cm, -20 cm), respectively. In this example, nineteen directions of the incident plane waves are used with nineteen directions of the received waves per each incidence (16). A step of 10 deg. is used. This configuration results in 361 synthetic data at each frequency. Six frequencies are used in the frequency hopping scheme as 10 MHz, 200 MHz, 500 MHz, 1 GHz, 3 GHz and 5 GHz. The initial guess of the two unknowns is assumed a circular cylinder of the radius of $r_c = 10\,\text{cm}$ centered at $(x_c, y_c) = (40\,\text{cm}, 0)$ (see Fig. 6(a)). The frequency hopping technique is combined with the level set method to avoid dropping the algorithm in local minima as explained in [21, 33]. Lower frequencies of 10 MHz and 200 MHz were employed at the beginning of the frequency hopping scheme to find the targets' locations, followed by relatively higher frequencies

to retrieve the details of the objects. Notice the progress of the reconstruction versus the frequency shown in Fig. 6. Notice also that the computational domain should include the initial guess, the two targets with adequate space for the evolving objects. In this work, the computational domain is a square with the dimensions of 80 cm centered at (40 cm, 0).

Figure 5 shows the normalized cost function versus the inversion iterations. The cost function is normalized with respect to the synthetic data at each frequency. The expression of the cost function is given as:

$$\text{Cost function} = \frac{\sum_{i=1}^{N_{inc}} \sum_{j=1}^{N_{meas}^{i}} \left\| E_{z,sim}^{sc}(\theta_i^{inc}, \theta_{ij}^{meas}) - E_{z,meas}^{sc}(\theta_i^{inc}, \theta_{ij}^{meas}) \right\|^2}{\sum_{i=1}^{N_{inc}} \sum_{j=1}^{N_{meas}^{i}} \left\| E_{z,meas}^{sc}(\theta_i^{inc}, \theta_{ij}^{meas}) \right\|^2} \tag{21}$$

Due to the fact that the cost function at each frequency is not normalized to the previous value, the plots in Fig. 5 show jumps once the algorithm hops to a new frequency as discussed in [21–25]. The results in Fig. 5 show that the algorithm converged after about 7000 iterations with residual error of 0.02. The observed fluctuations in the cost function plot are not understood yet as they are noticed at lower and higher frequencies; however, they do not affect the final reconstructions. Fig. 6(a) shows the initial guess, Fig. 6(b) shows the reconstruction after 3700 iterations at 500 MHz, and Fig. 6(c) shows the reconstruction after 7000 iterations at 5 GHz. These results showed the capability of the level set algorithm when the two ellipses were located far from the wall.

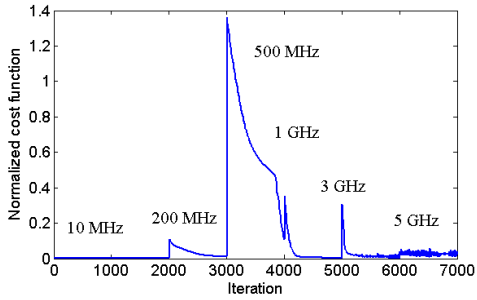

Figure 5. Normalized cost function for reconstruction of two elliptical cylinders ($d = 40$ cm).

Based on our results in 2D cases [24], using the low frequency of 10 MHz reduces the error between the simulated and measurement data. The deformation velocity is well-behaved and points towards the location of the target objects. A coarser discretization of the evolving contours is used in the lowest frequency compared with the higher ones. In free space case, the lowest frequency successfully helps retrieving the unknown location of the target [24]. The main problem arises due to the far-field criteria for collecting the measurement data in real applications.

The second case uses the same data of Figs. 5, 6 but with decreasing the distance to wall to $d = 20\,\text{cm}$ instead of $d = 40\,\text{cm}$. In this case, the two ellipses are located at (20 cm, 20 cm) and (20 cm, -20 cm), respectively. The same initial guess of Fig. 6 is assumed here. Fig. 7 shows the final reconstruction results. The cost function which demonstrates the convergence of the algorithm in this case (not shown here) is similar to that shown in Fig. 5.

To investigate the effect of the distance between the wall and the two ellipses on the reconstruction results, the same data of Fig. 6 is repeated except with more decrease of the distance to only $d = 8\,\text{cm}$. The same initial guess of Fig. 6 is used here. The final reconstruction

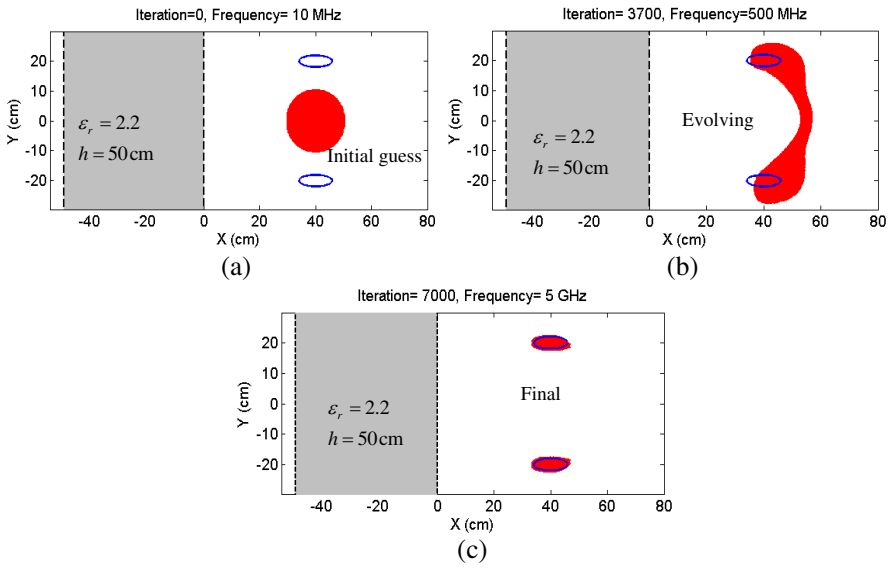

Figure 6. Reconstruction of two elliptical cylinders behind the dielectric wall when ($d = 40\,\text{cm}$). (a) Initial guess, (b) after 3700 iterations, (c) after 7000 iterations.

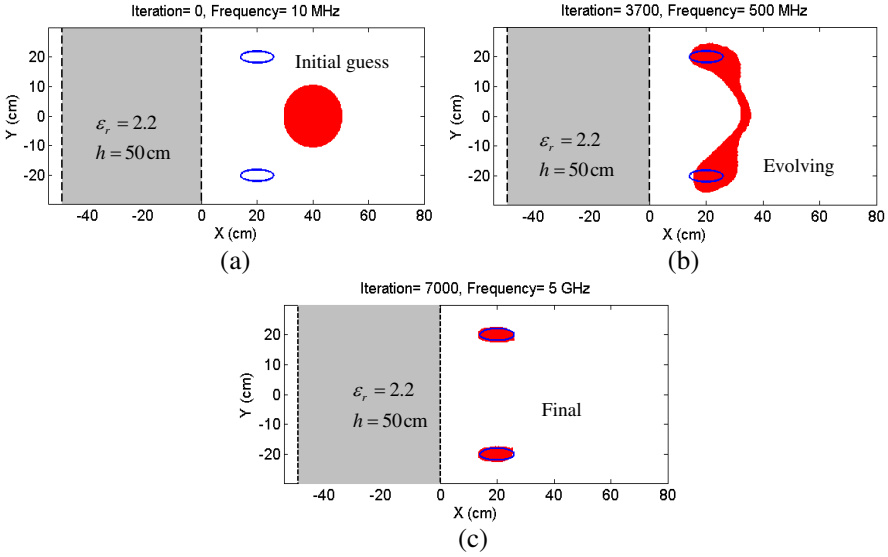

Figure 7. Reconstruction of two elliptical cylinders behind the dielectric wall when ($d = 20\,\text{cm}$). (a) Initial guess, (b) after 3700 iterations, (c) after 7000 iterations.

results are shown in Fig. 8. In this case, the cost function (not shown here) is similar to that shown in Fig. 5.

The results of Figs. 5–8 show that the level set reconstruction algorithm successfully retrieved the two ellipses even when the distance to the wall was 40 cm, 20 cm, and 8 cm. The CPU time required for the above examples was $\sim$ 40 minutes total. The SUN platform with AMD Opteron (tm) Processor 850 of 2393 MHz and 8 GB of RAM was used.

3.2. Reconstruction of a Defected Pipe

The reconstruction of a defected pipe hidden behind a wall is investigated as shown in Figs. 9 and 10. The length of the crack is 2.8 cm with width of 3 cm as depicted in Fig. 10. The defect is located on the surface of a circular pipe that has a radius of 10 cm and it is centered 60 cm away from the wall. The thickness of the wall is assumed 20 cm made of dry concrete of permittivity $\varepsilon_r = 4.5$ and loss tangent $\tan\delta = 0.0111$. The total number of synthetic data used in this example is the same with 19 incident and 19 scattering directions per each incidence (16). The same initial guess of Fig. 6 is used here with four different location of the defected pipe as shown in Figs. 10(a)–(d).

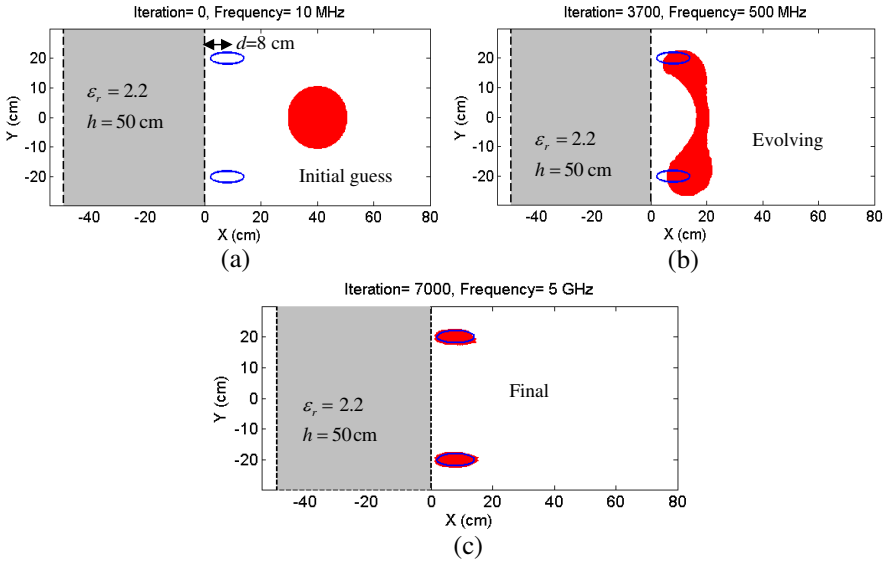

Figure 8. Reconstruction of two elliptical cylinders behind the dielectric wall when ($d = 8$ cm). (a) Initial guess, (b) after 3700 iterations, (c) after 7000 iterations.

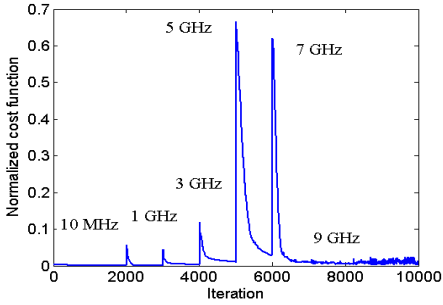

Figure 9. Normalized cost function for reconstruction of the defected pipe ($d = 60$ cm).

In this case, six frequencies are used in the frequency hopping scheme as 10 MHz, 1 GHz, 3 GHz, 5 GHz, 7 GHz and 9 GHz. The normalized cost function is shown in Fig. 9 which clearly shows the convergence of the algorithm after 9990 Iterations. The results in Figs. 10(a)–(c) show satisfactory results of the defected pipe; however Fig. 10(d) did not show a good reconstruction of the defect due to the

increased multiple scattering with the wall at the reduced distance in this case. The higher frequencies 5 GHz, 7 GHz and 9 GHz are needed to retrieve the defect in the pipe as shown in Figs. 10(a)–(c), although the transmission coefficient in the wall was reduced to 0.71, 0.63, 0.53, respectively, at these frequencies when considering the wall alone.

The results show that as the distance to the wall decreases, the reconstructed profile starts to deteriorate. In the last case, when the crack is only 1 cm away from the dielectric wall, it was not retrieved successfully as shown in Fig. 10(d). This can be explained by the fact that the multiple scattering between the wall and the object increases leading to inaccurate calculations using the stationary phase method. On the other hand, when the same defected pipe is placed in free space, the defect was perfectly reconstructed as reported in [24] where frequencies up to 15 GHz were used. The reconstruction time for the cases of Fig. 10 was ~ 4 hours total on the same SUN platform.

It is known that inverting limited view data imposes a challenge on the reconstruction accuracy. However, the level set has shown a success in reconstructing the shape and location of targets using limited view data compared with other methods such as the linear sampling method [19, 23]. For example, in the reconstruction of a defected pipe

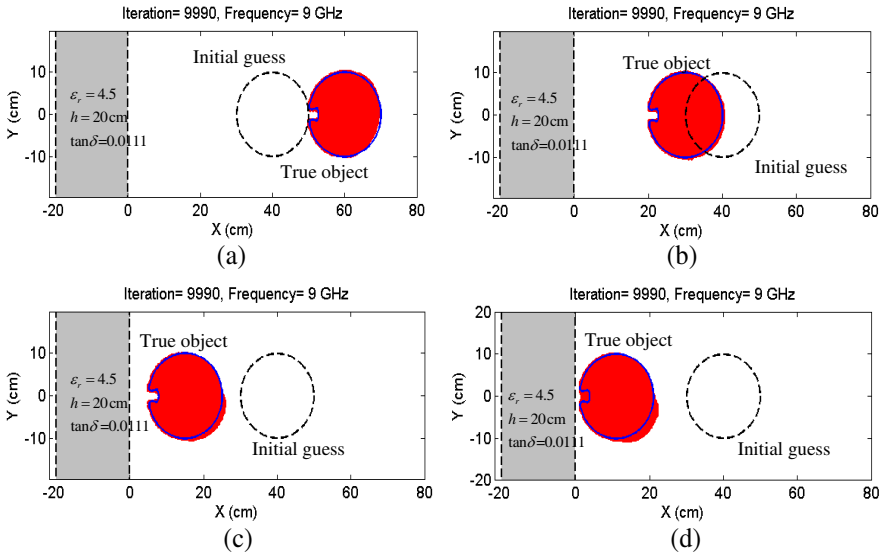

Figure 10. Reconstruction of the defected pipe at different distances from the wall. (a) $d = 40$ cm, (b) $d = 30$ cm, (c) $d = 15$ cm, (d) $d = 11$ cm.

in free space when illumination was available at one direction, the level set was successful in retrieving a partial profile of the defect [24].

3.3. Reconstruction of the Three Objects Using Noisy Data

In this example, the reconstruction of three objects of arbitrary cross-sections is shown when noisy data was added. This example deals with an unsymmetrical structure of the objects behind the wall. The objects are rectangular cylinder, triangular cylinder, and elliptical cylinder. The thickness of the wall is assumed 20 cm with permittivity of $\varepsilon_r = 9.0$ and loss tangent $\tan\delta = 0.0111$. The same number of data and the same initial guess are used here. Two different noise levels are examined in this example with the signal to noise ratio (SNR) SNR $= 20\log(\frac{E^{rms}_{signal}}{E^{rms}_{noise}})$, where E^{rms}_{signal} and E^{rms}_{noise} represent the root-mean-square of the signal and the Gaussian noise, respectively. A fixed SNR is used at all frequencies which mean that the level of the noise depends on the amplitude of the synthetic data which is changing with frequency. In this case, nine frequencies are used in the frequency hopping scheme as 10 MHz, 100 MHz, 200 MHz, 500 MHz, 750 MHz, 1 GHz, 3 GHz, 5 GHz and 7 GHz.

As mentioned earlier, the lower frequencies helped to retrieve the general profile of the targets while the higher frequencies helped to reconstruct the details of the three objects. The normalized cost function is shown in Fig. 11.

The reconstruction results of the three targets using noisy data corresponding to SNR = 10 dB are shown in Fig. 12(a), in Fig. 12(b) after 6500 iterations at 200 MHz, and in Fig. 12(c) after 24000 iterations at 7 GHz showing the final reconstruction.

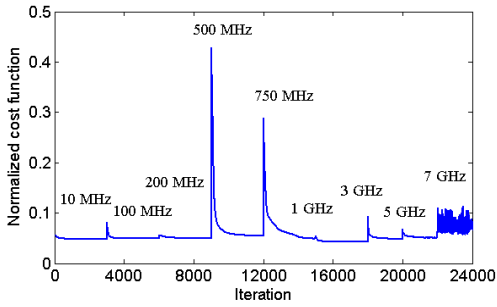

Figure 11. Normalized cost function for reconstruction of the three objects (SNR = 10 dB).

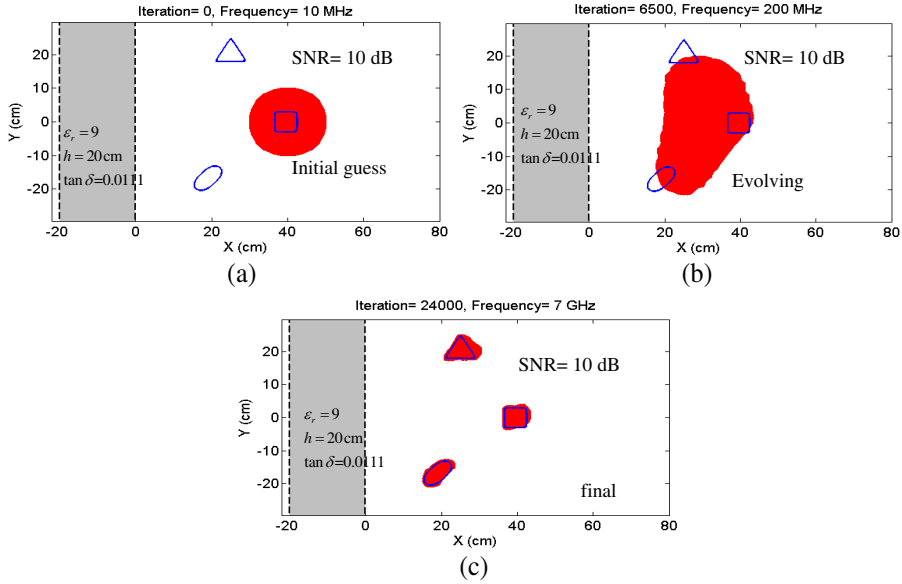

Figure 12. Noisy data of SNR = 10 dB. (a) Initial guess, after (b) 6500 iterations and (c) 24000 iterations.

Despite the noisy data and the limited view configuration of the incident and scattering directions, the level set algorithm successfully retrieves the three objects behind the wall with a single initial guess. However since there is no illumination from the right side of the wall, the reconstructed profile is a little bit distorted on that side. Due to the more complex configuration in this example, larger number of frequencies and iterations were needed compared with the previous examples. The same case is repeated but when the data is more noisy with SNR = 5 dB. The results show less satisfactory reconstructed shapes due to the higher level of noise (not presented here). The CPU time was $\sim$ 3 hours for 24000 iterations on the same SUN platform.

The number of employed frequencies is increased according to the complexity of the targets objects. In the example of Fig. 11, the number of frequencies is increased (9 frequencies) compared with the earlier examples (6 Frequencies). However, using more frequencies does not degrade the reconstructed profile but leads to increasing the required CPU time. In general, the working frequency should jump to a higher one, when the cost function drops in local minima and no further details of the target is retrieved using the data at the current frequency. In this work, a pre-assigned number of iterations

(mostly 1000 iterations) are used, while in [23], the stagnancy of the cost function is used as a signal for the frequency hopping. The later scheme avoids the increased CPU time when the cost function drops in local minima. In [23], the scheme was based on collecting the most recent 20 samples of the cost function and implementing the average window technique of each five samples. If the difference between the averages is less than a threshold (e.g., 1%), the algorithm hops to the higher frequency.

3.4. Parallelization of the Reconstruction Algorithm

In general, the problem of the shape reconstruction in the stratified media is more computationally intensive compared with the free space case. Therefore, it is necessary to implement algorithm parallelization to speed up the computations. Using the MPI parallelization, the computational load is distributed between several processors. The level set algorithm was parallelized for the reconstruction of multiple 2D PEC objects immersed in free space [22] with achieved maximum speedup range of 53X to 84X using 256 processors on the San Diego Super Computer Center (SDSC) facilities. In this work, the parallelized code is tested on the National Center for Supercomputing Applications (NCSA) at the University of Illinois. NCSA TeraGrid IA-64 Linux Cluster is employed to run the code. The machine consists of 887 IBM cluster nodes: 256 nodes with dual 1.3 GHz Intel® Itanium® 2 processors.

The parallelized algorithm in [22] is modified here to accommodate the Green's function in stratified media (4). The parallelization is based on three main bottlenecks; (i) the domain decomposition approach for updating the level set function in the whole computational domain, (ii) the distribution of calculating the deformation velocity, and (iii) the inversion of the MoM impedance matrix using Scalapack library available on NCSA supercomputers. The details of these bottlenecks are reported and discussed in [22].

The parallelized level set algorithm using different number of processors is tested to obtain the same reconstruction results of Fig. 12. The reconstruction CPU time consumed after 24000 inversion iterations using a single processor is ~ 7.5 hours while it is 15minutes when using 128 processors leading to achieve a maximum speedup of 29X as shown in Fig. 13. The corresponding parallelization efficiency is $\sim$ 22% in this case as shown in Fig. 14. Note that speedup is defined as the CPU time when using a single processor divided by the CPU time when using multiple processors on the same platform. The parallelization efficiency quantitatively describes the effectiveness of the parallelized code and is defined as the speedup divided by the

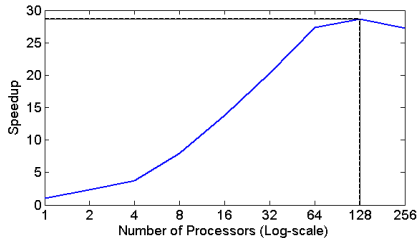

Figure 13. Speedup vs. the number of processors.

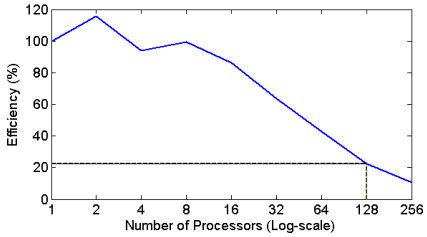

Figure 14. Efficiency vs. number of processors.

number of processors [22]. The result of Fig. 13 shows a maximum speedup of ~ 29 when using 128 processors; however, more increasing of the number of processors was not helpful due to the overhead in the communications and other factors as discussed in [22]. The maximum number of 256 processors is used to show the decrease in the speed up curve in Fig. 13. It is important to emphasize that the presented algorithm is not limited to symmetric simple shapes of the targets or to the 2-D configurations as reported in [23]. Also the algorithm was tested successfully on both TM and TE polarizations [21, 25].

4. CONCLUSIONS

The Level set algorithm is implemented to reconstruct the shape and location of multiple 2-D PEC objects hidden behind a dielectric wall with *a priori* known parameters. The stationary phase method is implemented to approximate the Sommerfeld integrals to speed up the calculations and to avoid the inaccuracy generated due to the arbitrary truncation in the integration limits when numerically evaluating the full Green's function. The results demonstrate that the level set method is capable of reconstructing the shapes and locations of multiple objects hidden behind a wall even with (i) limited view data, (ii) corrupted data up to SNR = 10 dB, and (iii) near proximity to the wall. More investigations are necessary to increase the accuracy of the algorithm when reconstructing fine features in targets located very close to the wall. Also more work is needed when the wall's parameters are not *a priori* known.

REFERENCES

1. Lu, T., K. Agarwal, Y. Zhong, and X. Chen, "Through-wall imaging: Application of subspace-based optimization method,"

Progress In Electromagnetics Research, Vol. 102, 351–366, 2010.

2. Maaref, N., P. Millot, X. Ferrières, C. Pichot, and O. Picon, "Electromagnetic imaging method based on time reversal processing applied to through-the-wall target localization," *Progress In Electromagnetics Research M*, Vol. 1, 59–67, 2008.
3. Soldovieri, F., R. Solimene, and R. Pierri, "A simple strategy to detect changes in through the wall imaging," *Progress In Electromagnetics Research M*, Vol. 7, 1–13, 2009.
4. Rekanos, I. T. and A. Räisänen, "Microwave imaging in the time domain of buried multiple scatterers by using an FDTD-based optimization technique," *IEEE Transactions on Magnetics*, Vol. 39, No. 3, 1381–1384, May 2003.
5. Travassos, X. L., D. A. G. Vieira, N. Ida, C. Vollaire, and A. Nicolas, "Inverse algorithms for the GPR assessment of concrete structures," *IEEE Transactions on Magnetics*, Vol. 44, No. 6, 994–997, June 2008.
6. Borek, S. E., "An overview of through the wall surveillance for homeland security," *Proceedings of the 34th Applied Imagery and Pattern Recognition Workshop (AIPR05)*, 2005.
7. Soldovieri, F. and R. Solimene, "Through-wall imaging via a linear inverse scattering algorithm," *IEEE Geo. and Rem. Sens. Letters*, Vol. 4, No. 4, 513–517, October 2007.
8. Dehmollaian, M. and K. Sarabandi, "Refocusing through building walls using synthetic aperture radar," *IEEE Transactions on Geoscience and Remote Sensing*, Vol. 46, No. 6, 1589–1599, June 2008.
9. Hantscher, S., A. Reisenzahn, and C. G. Diskus, "Through-wall imaging with a 3-D UWB SAR algorithm," *IEEE Signal Processing Letters*, Vol. 15, 269–272, 2008.
10. Song, L. P., C. Yu, and Q. H. Liu, "Through-wall imaging (TWI) by radar: 2-D tomographic results and analyses," *IEEE Transactions on Geoscience and Remote Sensing*, Vol. 43, No. 12, December 2005.
11. Ahmad, F., Y. Zhang, and M. G. Amin, "Three-dimensional wideband beamforming for imaging through a single wall," *IEEE Geo. and Rem. Sens. Letters*, Vol. 5, No. 2, 176–179, April 2008.
12. Pierri, R., G. Prisco, F. Soldovieri, and R. Solimene, "Three-dimensional through-wall imaging under ambiguous wall parameters," *IEEE Transactions on Geoscience and Remote Sensing*, Vol. 47, No. 5, 1310–1317, May 2009.
13. Wang, G. and M. G. Amin, "Imaging through unknown walls

using different standoff distances," *IEEE Trans. Signal Process.*, Vol. 54, No. 10, 4015–4025, October 2006.

14. Debes, C., M. G. Amin, and A. M. Zoubir, "Target detection in single- and multiple-view through-the-wall radar imaging," *IEEE Transactions on Geoscience and Remote Sensing*, Vol. 47, No. 5, 1349–1361, May 2009.
15. Yacoub, H. and T. K. Sarkar, "A homomorphic approach for through-wall sens.," *IEEE Transactions on Geoscience and Remote Sensing*, Vol. 47, No. 5, 1318–1327, May 2009.
16. Yoon, Y. S. and M. G. Amin, "Spatial filtering for wall-clutter mitigation in through-the-wall radar imaging," *IEEE Transactions on Geoscience and Remote Sensing*, Vol. 47, No. 9, 3192–3208, September 2009.
17. Soldovieri, F., R. Solimene, and G. Prisco, "A multiarray tomographic approach for through-the wall imaging," *IEEE Transactions on Geoscience and Remote Sensing*, Vol. 46, No. 4, 1192–1199, April 2008.
18. Soldovieri, F., A. Brancaccio, G. Leone, and R. Pierri, "Shape reconstruction of perfectly conducting objects by multiview experimental data," *IEEE Transactions on Geoscience and Remote Sensing*, Vol. 43, No. 1, 65–71, January 2005.
19. Catapano, L. and L. Crocco, "An imaging method for concealed targets," *IEEE Transactions on Geoscience and Remote Sensing*, Vol. 47, No. 5, 1301–1309, May 2009.
20. Ramananjaona, C., M. Lambert, D. Lesselier, and J.-P. Zol'esio, "Shape reconstruction of buried obstacles by controlled evolution of a level set: from a min–max formulation to numerical experimentation," *Inverse Problems*, Vol. 17, 1087–1111, 2001.
21. Hajihashemi, M. R. and M. El-Shenawee, "TE versus TM for the shape reconstruction of 2-D PEC targets using the level-set algorithm," *IEEE Transactions on Geoscience and Remote Sensing*, Vol. 48, No. 3, 1159–1168, March 2010.
22. Hajihashemi, M. R. and M. El-Shenawee, "High performance computing for the level-set reconstruction algorithm," *Journal of Parallel and Distributed Computing*, Vol. 70, No. 6, 671–679, June 2010.
23. Hajihashemi, M. R., "Inverse scattering level set algorithm for retrieving the shape and location of multiple targets," Ph.D. Dissertation, University of Arkansas, 2010.
24. Hajihashemi, M. R. and M. El-Shenawee, "Shape reconstruction using the level set method for microwave applications," *IEEE*

Antennas and Wireless Propagation Letters, Vol. 7, 92–96, 2008.

25. Hassan, A. M., M. R. Hajihashemi, D. A. Woten, and M. El-Shenawee, "Drift de-noising of experimental TE measurements for imaging 2D PEC cylinders," *IEEE Ant. and Wireless Propagation Letters*, Vol. 8, 1218–1222, 2009.
26. Wait, J. R., *Electromagnetic Waves in Stratified Media*, IEEE Press, 1996.
27. Cui, T. J. and W. Wiesbeck, "TM wave scattering by multiple two-dimensional scatterers buried under one-dimensional multi-layered media," *Proc. IEEE International Geo. and Rem. Sens. Symposium*, 27–31, Lincoln, May 1996.
28. Sethian, J. A., *Level Set Methods and Fast Marching Methods*, Cambridge University Press, 1999.
29. Osher, S. J. and R. P. Fedkiw, *Level Set Methods and Dynamic Implicit Surfaces*, Springer-Verlag, 2003.
30. Roger, A., "Reciprocity theorem applied to the computation of functional derivatives of the scattering matrix," *Electromagnetics*, Vol. 2, No. 1, 69–83, 1982.
31. Chew, W. C., "A quick way to approximate a sommerfeld-weyl-type integral," *IEEE Trans. on Antennas and Propagation*, Vol. 36, No. 11, 1654–1657, November 2008.
32. FEKO User's manual, Suite 5.3, July 2007.
33. Chew, W. C. and J. H. Lin, "A frequency-hopping approach for microwave imaging of large inhomogeneous bodies," *IEEE Microwave and Guided Wave Letters*, Vol. 5, No. 12, 439–441, December 1995.
34. Aksun, M. I., "A robust approach for the derivation of closed-form Green's functions," *IEEE Trans. Microwave Theory Tech.*, Vol. 44, 651–658, May 1996.